Tuneable and reversible O redox in 4d transition metal oxides for high potential Na ion batteries

M. Hussein N. Assadi,[a,b,*] Marco Fronzi,[c,d] Mike Ford[c] and Yasuteru Shigeta[a]

[a]Center for Computational Sciences, University of Tsukuba, Tennodai 1-1-1, Tsukuba, Ibaraki 305-8577, Japan.

[b]Center for Green Research on Energy and Environmental Materials (GREEN), National Institute for Materials Science (NIMS), 1-1 Namiki, Tsukuba, Ibaraki 305-0044, Japan.

[c]International Research Centre for Renewable Energy, State Key Laboratory of Multi- phase Flow in Power Engineering, Xi'an Jiaotong University, Xi'an 710049, Shaanxi, China.

[d]School of Mathematical and Physical Science, University of Technology Sydney, Ultimo 2007, New South Wales 2007, Australia.

[*]Email: h.assadi.2008@ieee.org

ABSTRACT. Utilising reversible oxygen redox in Na and transition metal oxides offers unprecedented opportunities for designing high voltage, high capacity and affordable cathodes for rechargeable Na ion battery applications. Through judicious materials search and theoretical investigations, we identified new compounds with excellent energy storage properties that rely on oxygen states for charge compensation during the redox reaction. $Na_{4-x}Zr_5O_{12}$ with a voltage of 3.583 V and $Na_{1-x}Pd_2PO_3$ voltage of 2.630 V experience a meagre volume change of ~1% during the sodiation/desodiation process. Because of this minor volume change, these compounds are suitable for all-solid-state battery applications. Furthermore, $Na_{2-x}MoO_4$ shows a voltage of 4.743 V and an energy density of ~617.3 Wh/Kg. These values exceed the performance of most commercialised Na ion cathode materials. Examining the electronic structure of these compounds reveals that O states are always present at the top of valence band regardless of 4d transition metal species or its oxidation states. This feature is attributed to the more substantial 4d-2p hybridisation over the entire valence band which also prevents the bonding of oxidised O ions in the desodiated compounds preventing irreversible oxygen loss.

Keywords: DFT, Na ion battery, O redox

INTRODUCTION

Advancement in the secondary ion batteries has enabled the revolution in the consumer electronics[1, 2] and new vehicular technologies[3, 4] in the past two decades. The traditional paradigm of most common Li-ion batteries is based on the availability of multiple oxidation states of cationic transition metal (TM) in the cathode that enables the insertion and extraction of Li-ion which acts as an ionic charge carrier.[5, 6] New paradigms in designing cathode materials, however, should bypass both the use of Li as an ionic charge carrier and cationic redox as the sole charge compensation mechanism. That is because there is a pressing urge to substitute Li with a more affordable and accessible alkali metal such as Na.[7-9] Anionic redox, should also be seriously considered to reduce the costs associated with the TM elements such as Co and increase the capacity beyond the limits of the cationic redox. For long, anionic redox was generally thought to be detrimental to the lifecycle of the cathode as it would trigger irreversible oxygen loss in oxide cathode materials.[10-13] Recently, however, reversible anionic redox has been proposed and observed in cation-disorder and Li excess oxides.[14-17]

The availability of oxygen redox opens new and unique opportunities in designing cathode materials that are made of Na ion and fifth (4d) row TM ions. Since 4d electrons are spatially more spread compared to their 3d counterparts, their hybridisation with O 2p states in the valence band is generally greater.[18, 19] The greater 2p-4d hybridisation, in turn, can make the O 2p states more labile for redox reaction and may also prevent the irreversible O loss. Furthermore, TM oxides in which the TM adopts d^0 configuration which have long been considered electrochemically inactive[20-23] can be principally utilised in a new class of cathodes materials that exhibit O only redox mechanism.

We, here, investigate the reversible oxygen redox in novel 4d TM and Na oxides with excellent electrochemical properties. These compounds are $Na_4Zr_5O_{12}$, Na_1NbO_2, Na_2MoO_4,

$Na_1Pd_2O_3$ and Na_3AgO_2. Na_1NbO_2 (Ref. 24), Na_2MoO_4 (Ref. 25)and Na_3AgO_2 (Ref. 26) have been previously synthesised while $Na_4Zr_5O_{12}$ and $Na_1Pd_2O_3$ are modelled based on the K containing compounds $K_4Zr_5O_{12}$ (Ref. 27, 28) and KPd_2O_3 (Ref. 29). By careful density functional examination of the redox reaction in these compounds, we will draw a comprehensive picture of O redox activity in 4d TM and Na oxides.

METHODS

Spin-polarized density functional theory (DFT) calculations were carried out using augmented plane-wave method as implemented in VASP.[30, 31] The energy cut-off was set to 550 eV, while a k-point mech was produced by Monkhorst Pack scheme with a spacing of ~0.02 $Å^{-1}$ for Brillouin zone sampling. Hubbard term U_{eff} = 2 eV was added to the 3d electrons to improve the accuracy of the electronic description through GGA+U approach.[32] Electronic population localised at the ionic centres were analysed with Bader code.[33] Bader charge analysis provide us with the change in the electronic population at ionic centres during the sodiation/desodiation process. Bonding characteristics were examined using Lobster code.[34] Lattice parameters, internal atomic coordinates and magnetic moment of the TM ions of all compounds were allowed to fully relax.

We calculated the average potential using the following equation:

$$V = \frac{[E^t(sodiated) - E^t(\text{desodiated}) - nE^t(Na)]}{-ne} \qquad \text{Equation 1}$$

in which E^t is the DFT total energy, n is the number of the removed Na ions during the desodiation process, and e is the electronic charge. Further details on the computational settings and the justification of the settings are presented in the Supplementary Information. The irreducible primitive cell of Na_1NbO_2 and $Na_4Zr_5O_{12}$ were used for the calculations. For Na_2MoO_4, $Na_6Pd_{12}O_{18}$ and $Na_{12}Ag_4O_8$, the conventional unicells were used. The chemical

composition of the unitcells of the considered compounds were Na_4Zr5O_{12}, $Na_2Nb_2O_4$, $Na_8Mo_4O_{16}$, $Na_6Pd_{12}O_{18}$ and $Na_{12}Ag_4O_8$.

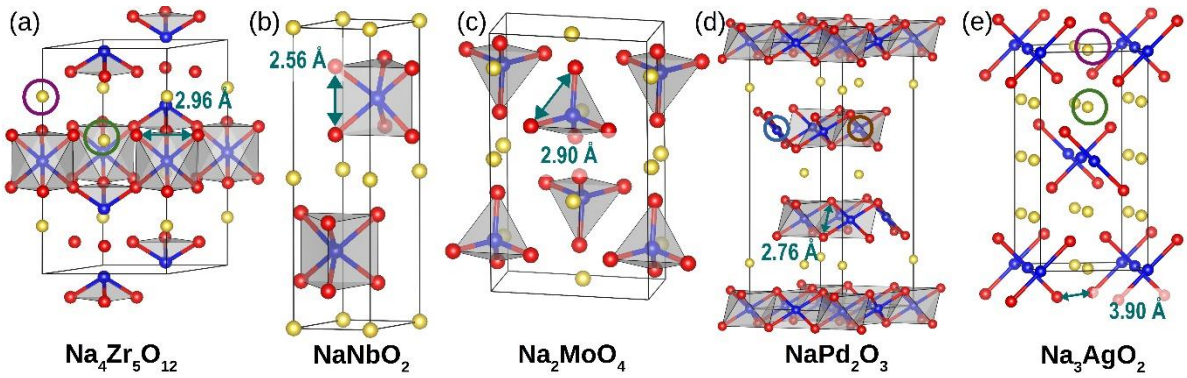

Figure 1. The schematic representation of the sodiated compounds. The blue, red and yellow spheres correspond to TM, oxygen and sodium ions. The green and purple circles in (a) and (e) mark two distinct crystal sites occupied by Na ions. See Table 1 for more details. The blue and brown circles in (d) mark the planar and octahedral Pd ions respectively. The shortest O-O distance is also marked with green double arrows.

RESULTS AND DISCUSSIONS

The calculated lattice parameters and the Wyckoff position of the constituting elements for sodiated compounds are given in Table 1. For those compounds that have been experimentally characterised, the calculated values deviate from the experimental values by ~1% (Tables S1 and S2) indicating excellent convergence of the computational settings.

Table 1. The calculated lattice parameters and characteristics of the sodiated compounds.

	$Na_4Zr_5O_{12}$	Na_1NbO_2	Na_2MoO_4	$Na_1Pd_2O_3$	Na_3AgO_2
Lattice Group	164 ($P\bar{3}m1$)	194 ($P6_3/mmc$)	12 ($C2/m$)	160 ($R3m$)	72 ($Ibam$)
a (Å)	5.855	3.013	11.692	6.130	5.525
b (Å)	5.855	3.013	5.945	6.130	11.031
c (Å)	10.652	11.708	6.942	16.897	6.002
α (°)	90.000	90.000	90.000	90.000	90.000
β (°)	90.000	90.000	117.647	90.000	90.000
γ (°)	120.000	120.000	90.000	120.000	90.000
Volume ($Å^3$)	316.243	92.052	427.418	549.896	365.826
Na Wycoff Site	2d, 2c	2a	4i	6c	4b, 8g
TM Wycoff Site	1a, 2d	2d	4i	9e, 3d	4b
O Wycoff Site	12j	4f	4i	36i	8j

Na ions in $Na_4Zr_5O_{12}$ occupy two distinct 2d and 2c Wyckoff sites which are marked by purple and green circles respectively in Figure 1(a). To identify which Na ions vacate during the desodiation process, we calculated the formation energy of Na vacancy (V_{Na}) from both sites. We found that formation energy of V_{Na} from the 2d site which was −3.570 eV to be

lower than that of the 2c site which was −3.392 eV. Accordingly, in the desodiated compound, all Na ions were removed from the 2d site. Similarly, in $Ibam$ Na_3AgO_2, as marked in Figure 1(e), one third of the Na ions occupy the 4b sites while two thirds of the Na ions occupy 8g sites, marked with purple and green circles respectively. The formation energy of V_{Na} from the 4b site being −2.554 eV was smaller than that of 8g the site which was −2.262 eV. As a result, the desodiation process was set to exhaust all the Na ions in 4d Wyckoff sites.

The lattice parameters of the desodiated compounds are given in Table 2. The desodiation process conserves the symmetry of the desodiated lattices except for Na_1NbO_2. The Na ion ordering in desodiated $Na_{0.5}NbO_2$ is similar to the Na ordering in P2 $Na_{0.5}CoO_2$ (Ref. 35) in which the Na ions are arranged in a superstructure with $\sqrt{2}a \times \sqrt{2}a$ periodicity, occupying octahedral sites with respect to the O ions. The unitcell of the desodiated $Na_{0.5}NbO_2$ has a chemical composition of $Na_2Nb_4O_8$. As seen in the first row of the Table 3, during the redox reaction, $Na_{4-x}Zr_5O_{12}$ and $Na_{1-x}Pd_2O_3$ show a negligible volume change ($\Delta V/V$) of ~1%. The small volume change in these materials make $Na_{4-x}Zr_5O_{12}$ and $Na_{1-x}Pd_2O_3$ suitable for all-solid-state battery applications.[36, 37] $Na_{1-x}NbO_2$ and $Na_{3-x}AgO_2$ show a moderate ~6% volume change during the sodiation/desodiation process while the largest volume change occurs in $Na_{2-x}MoO_4$ which was −15.310%.

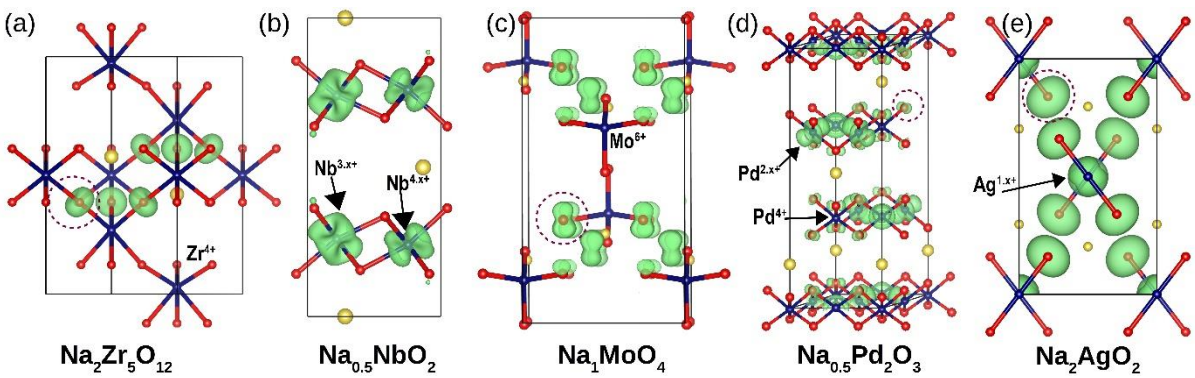

Figure 2. The schematic representation of the desodiated compounds. The iso-surfaces correspond to the spin density around the ions. Spin bearing O ions, marked with dashed circles, are those participating in the redox reaction. The blue, red and yellow spheres correspond to TM, oxygen and sodium ions respectively.

Table 2. The calculated lattice parameters and characteristics of the desodiated compounds.

	$Na_2Zr_5O_{12}$	$Na_{0.5}NbO_2$	Na_1MoO_4	$Na_{0.5}Pd_2O_3$	Na_2AgO_2
Lattice Group	164 ($P\bar{3}m1$)	25 ($Pmm2$)	12 ($C2/m$)	160 ($R3m$)	72 ($Ibam$)
a (Å)	5.855	3.107	11.601	6.081	5.868
b (Å)	5.855	3.107	6.194	6.081	9.979
c (Å)	10.627	11.888	6.870	17.346	5.904
α (°)	90.000	90.000	90.000	90.000	90.000
β (°)	90.000	90.000	93.282	90.000	90.000
γ (°)	120.000	90.000	90.000	120.000	90.000
Volume (Å^3)	315.500	98.793	492.855	555.504	345.770
Removed Na site	2d	2a	4i	6c	4b

The second, third and fourth rows of Table 3 show the electrochemical performance of the cathode materials. The highest potential belongs to Na_xMoO_4 and Na_xZr5O_{12} which is ~4.7 V and ~3.6 V respectively. The potential of the rest of compounds averages around ~2.5 V. The specific capacity which is proportional to the number of Na ions removed over the molecular mass is ~130 mAh/g for Na_xMoO_4 and Na_xAgO_2. Given its high potential, Na_xMoO_4, therefore, emerges as high potential and a relatively high capacity cathode material. This point is reflected in the outstanding energy density of ~617 Wh/Kg which exceeds some of the highest density Na ion cathodes such as $Na_2Fe_2(SO_4)_3$ with an energy density of 540 Wh/kg (Ref. 38) and $Na_{1.5}VPO_{4.8}F_{0.7}$ with an energy density of ~600 Wh/kg.[39]

Table 3. The electrochemical performance of the cathode materials. The nominal TM electronic configuration corresponds to the sodiated compounds.

	$Na_{4-x}Zr_5O_{12}$	$Na_{1-x}NbO_2$	$Na_{2-x}MoO_4$	$Na_{1-x}Pd_2O_3$	$Na_{3-x}AgO_2$
$\Delta V/V$	0.859	−7.324	−15.310	−1.020	5.482
Potential	3.583	2.476	4.743	2.630	2.398
Capacity (mAh/g)	72.430	90.613	130.155	47.214	128.335
Energy density (Wh/Kg)	259.487	224.372	617.295	124.182	307.793
Nominal TM configuration	d^0	$t_{2g}^2 e_g^0$	$4d^0$	$t_{2g}^6 e_g^0$, $e_g^4 a_{1g}^2 b_{1g}^2 b_{2g}^0$	d^{10}
TM hybridisation	Octahedral	Octahedral	Tetrahedral	Octahedral & Planar	Linear
Δe(TM) (e)	5×−0.0493	2×−0.3954 2×−0.2804	4×−0.0219	9×−0.1234[a] 3×−0.0463[b]	4×−0.315
Δe(O) (e)	6×−0.1763 6×−0.0783	4×−0.0663 4×−0.0148	8×−0.2976 8×−0.1402	18×−0.0779	8×−0.238

[a] Charge compensation corresponding to Pd^{2+}
[b] Charge compensation corresponding to Pd^{4+}

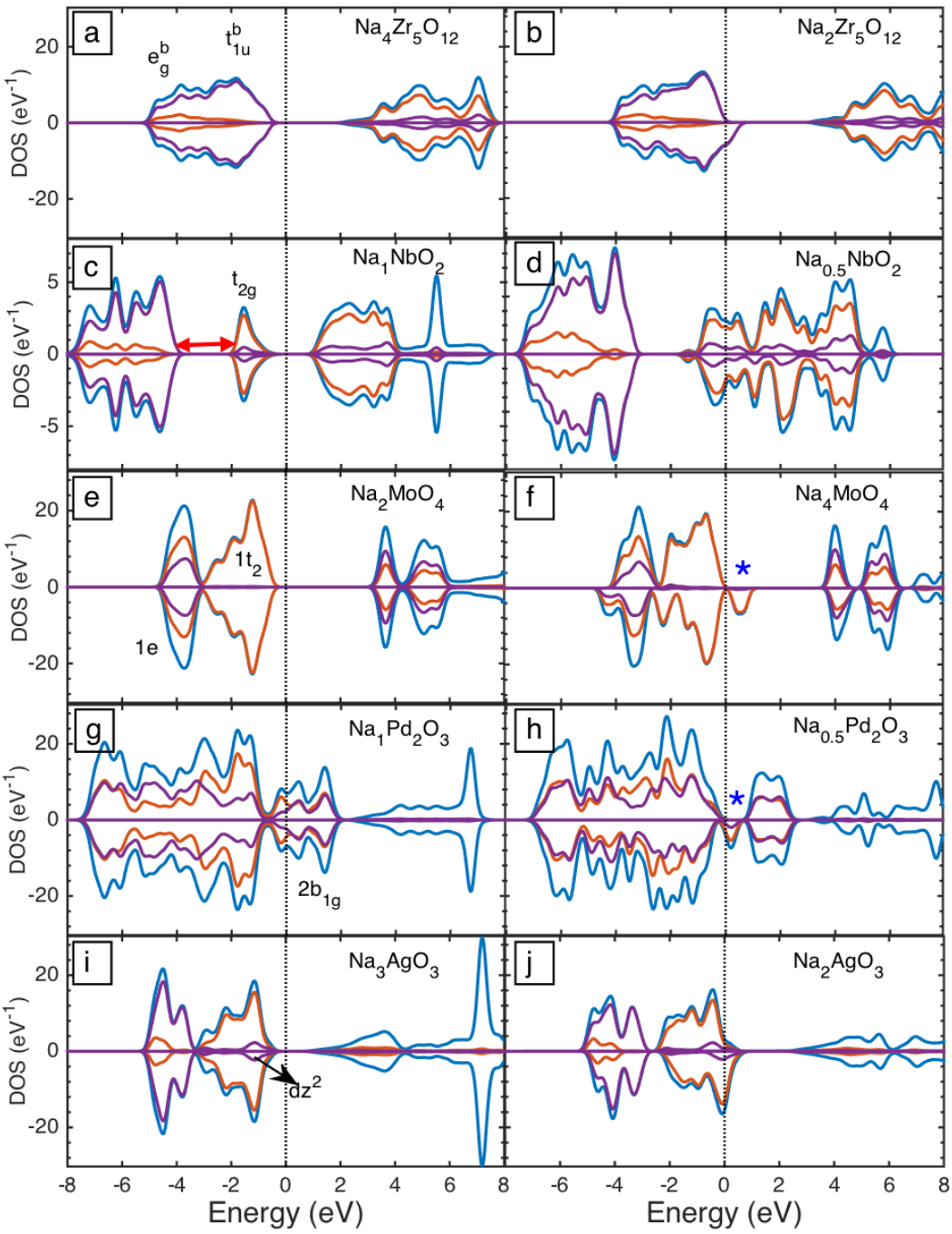

Figure 3. The total and partial density of states of the sodiated (left column) and desodiated compounds (right column). Blue, purple and orange lines represent total, O 2p and TM 4d partial states respectively.

Now let's examine the charge compensation mechanism during the desodiation process. We can rank the compounds according to the share of the TM and O to the charge compensation mechanism during sodiation/desodiation. In $Na_{1-x}NbO_2$, $Na_{1-x}Pd_2O_3$ and $Na_{3-x}AgO_2$, both TM and O ions participate in the charge compensation during the redox reaction. In the two

remaining compounds, $Na_{4-x}Zr_5O_{12}$ and $Na_{2-x}MoO_4$, the charge compensation dominantly originates from O electrons with minor participation from the TM ions.

In Na_xNbO_2, Nb^{3+}, upon desodiation, in a hypothetical ideal ionic picture, one Nb^{3+} ion would convert to a Nb^{4+} ion. However, in reality, the charge compensation is delocalised over all Nb ions. As seen Table 3, upon desodiation, every two out of the four Nb ions in the unitcell donate 0.3954 electrons while the other two Nb ions donate 0.2804 *e*. These Nb ions are denoted h $Nb^{3.x}$ and $Na^{3.y}$ respectively. Each O ion, on the other hand, donates a minuscule amount of 0.0405 *e*. As a result, the contribution of Nb and O to charge compensation amounts to 89.29% and 10.71% respectively. Figure 2(b) shows that how partially charged $Nb^{3.x}$ and $Nb^{3.y}$ are distributed in the desodiated compound. $Na_xPd_2O_3$ is another compound with significant TM redox participation. In $Na_1Pd_2O_3$, one fourth of Pd ions are octahedrally coordinated adopting a +4 oxidation states while the rest of the Pd ions are under planar coordination and adopt +2 oxidations state. As seen in Table 3, every planar Pd^{2+} ion, on average, compensates for 0.1234 *e* during the desodiation process. Octahedral Pd^{4+} and O participate in the redox reaction to a lesser extent by donating 0.0463 *e* and 0.0779 *e* respectively. Despite the contribution of any individual O ion to the redox reaction being rather small compared to that of Pd^{2+}, given that there are six O ions for every extracted Na ion, the total O contribution to the redox reaction exceeds that of the Pd ions. In this case, each of Pd^{2+}. Pd^{4+} and O contribute 41.87%, 5.24%, and 52.89% to the charge compensation respectively. Na_xAgO_2 also exhibits a mixed Ag and O redox during the desodiation process. In the desodiated system, Ag ions each compensates 0.3150 *e* while every O ion, on the other hand, offers 0.2380 *e*. Overall, Ag and O account for 24.85% and 75.15% of the electronic compensation during the redox reaction respectively.

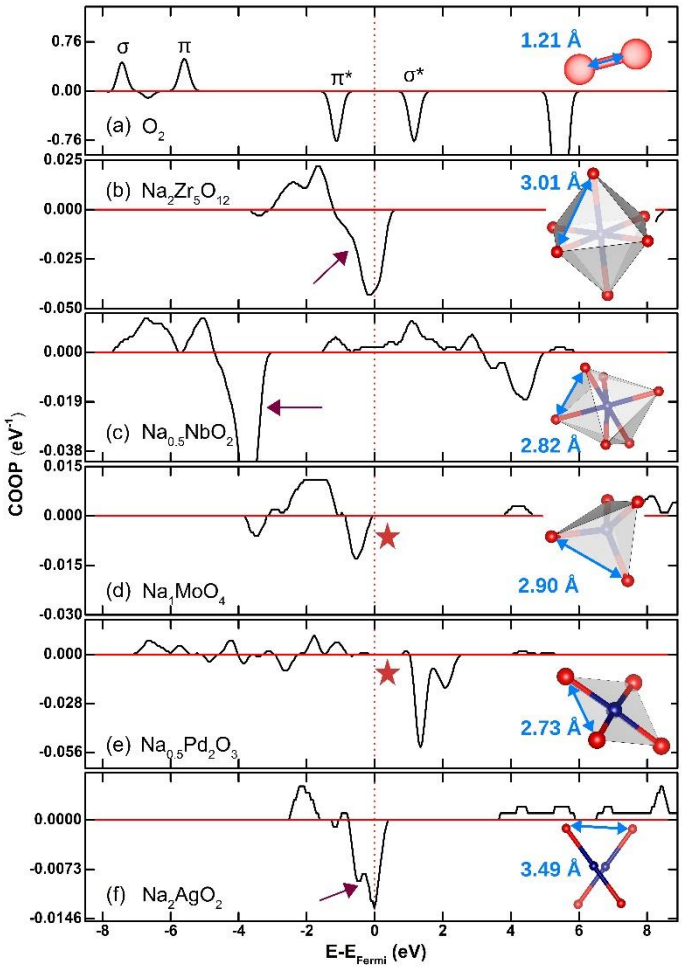

Figure 4.The crystal orbital overlap population (COOP) between the shortest O pairs in the desodiated compounds. The shortest O–O distance in each compound is shown in the insets. In (a) the COOP of O_2 molecule is given for presentation.

In $Na_xZr_5O_{12}$, six out of 12 O ions donate 0.1763 *e* while the other six O ions donate 0.0783 *e*. Each Zr ion, on the other hand, compensates 0.0493 *e*. Consequently, in $Na_xZr_5O_{12}$, 13.89 % redox is borne in Zr and 86.11 % of redox is borne on O ions. As seen in Figure 2(a), only half of the O ions in $Na_xZr_5O_{12}$ are oxidised during the desodiation process. The share of O redox is the greatest in $Na_{2-x}MoO_4$. In this compound, as shown in Figure 2(c), half of the O ions in the primitive cell contribute 0.2976 *e* to the redox reaction while the other half of the O ions contribute 0.1402 *e* towards the redox reaction. Each Mo ions, on the other hand, compensates 0.0219 *e* to the redox reaction. Consequently, Mo's and O's participation in the redox reaction accounts for 2.44% and 97.56% respectively. Figure 2(c)

shows how the O ions with greater contribution to the redox reaction are arranged in the unicell.

Examining the partial density of states (DOS) for sodiated and desodiated compounds, presented in Figure 3, elucidates the orbital origin of the compensating charge during the desodiation process. First, let's examine the DOS of those compounds with significant TM participation in the redox reaction. In Na_1NbO_2, as seen in Figure 3(c), the filled t_{2g} are localised in a sub-band below the Fermi level and are separated from the main valence band which is dominated by the O 2p states by a pseudo-gap of ~1.5 eV (marked with a red arrow). This pseudo-gap is caused by the strong trigonal distortion in this compound.[40] Nb's empty t_{2g} and e_g states, on the other hand, constitute the majority states of the conductions band. Due to a slight hybridisation between O 2p and Nb's electrons near the Fermi level (marked with a blue arrow in Figure 3(c)), O 2p states marginally participate in the redox reaction. In $Na_1Pd_2O_3$, Pd^{4+} under octahedral coordination adopts $t_{2g}^6 e_g^0$ configuration while Pd^{2+} under square planar hybridisation adopts $e_g^4 a_{1g}^2 b_{2g}^2 b_{1g}^0$ configuration. The top of the valence band is, however, occupied by the molecular $2b_{1g}$ states (marked with a red arrow in Figure 3(g)) which arise from the hybridisation between linear Pd^{2+}'s b_{1g} and O 2p states. The lability of the $2b_{1g}$ states therefore evokes the participation of both 4d and 2p electrons in the redox reaction (Marked with an asterisk in Figure 3(h)). Under octahedral coordination, Pd^{4+} states gravitate towards the bottoms of the valence band[41] and as a result are, to a large extent, electrochemically inactive. In Na_3AgO_2, as seen in Figure 3(i), the top of the valence band is formed of the molecular b_1 states that arise from the hybridisation of Ag's d_{z^2} states and O's σ states while the bottom of the valence band is populated by the rest of Ag states. As a result of this hybridisation, both Ag 4d and O 2p states are labile for redox reaction in $Na_{3-x}AgO_3$.

In d^0 compounds with O dominant redox $Na_4Zr_5O_{12}$ and Na_2MoO_4, the area below the Femi level is dominated by O states. As seen in Figure *3*(a), In $Na_4Zr_5O_{12}$, under octahedral coordination, the hybridisation between O 2p and Zr $4d_{x^2-y^2}$ and $4d_{z^2}$ states results in bonding e_g^b states that occupy the bottom of the valence band. e_g^b states generally have d character. Given the distance of the e_g^b states from the Fermi level, these states are electrochemically inert. Furthermore, the electrochemically labile state that are located just below the Fermi level are made of t_{1u}^b states that have O character and arise from the hybridisation between O 2p and Zr 5p states. The lability of O states for the redox reaction can be seen in Figure 3(b) where the t_{1u}^b states have lost the compensating electrons in the spin-up channel. In Na_2MoO_4, as shown in Figure 3(e) and (f), in the bottom of the valence band is occupied by the $1e$ states with 4d character and $1a_1$ states which arise from the hybridisation O 2p and Mo 5s states. The region below the Fermi level, on the other hand, is occupied by the $1t_2$ states that arise from the hybridisation between O 2p and Mo 5p states. Given their proximity to the Femi level, the $1t_2$ states become electrochemically labile and as marked with an asterisk in Figure 3(f), donate electrons from spin-down channel during the desodiation reaction.

To examine the possibility of O−O bond formation between the hole bearing O ions after desodiation, we calculated the crystal orbital overlap population (COOP) between neighbouring oxygen ions with the shortest distance. COOP's positive and negative values indicate bonding and anti-bonding states respectively. The COOP values are presented in Figure 4. We also present the COOP of gaseous O_2 in Figure 4(a) for the sake of comparison. We observed a negligibly weak O−O bonding between hole bearing O ions in all of the desodiated compounds. The weakness of O−O bonding can be inferred from the COOP values in the desodiated compounds which are ~30 times smaller than that of O_2 gas. Furthermore, since both bonding and antibonding states are occupied for those interacting O

ions, this week bonding between the hole bearing O ions is not stable and does not promote the evolution of the O_2 gas. In $Na_2Zr_5O_{12}$, $Na_{0.5}NbO_2$ and Na_2AgO_2 the antibonding states (Marked with red arrows in Figure 4(b), (c) and (f) are even more populated than the bonding states. In Na_1MoO_4 and $Na_{0.5}Pd_2O_3$, there is no overlap between the hole states (indicated with a star marks in Figure 4(d) and (e) that are created upon desodiation.

The weak O−O bonding interaction in these compounds can be attributed to two factors; first, the desodiation process does not significantly alter the distance between closest O−O pairs except in $Na_{3-x}AgO_3$. By comparing the shortest O−O distances of the sodiated and desodiated compounds that are presented in Figure 1 and Figure 4 respectively, we find that the shortest O−O distance increases by 0.05 Å, in $Na_{4-x}Zr_5O_{12}$ and 0.26 Å in $Na_{1-x}NbO_2$ while it remains unchanged in $Na_{2-x}MoO_4$. This distance, nonetheless, shows a minor decrease of 0.03 Å in $Na_{1-x}Pd_2O_3$ and a moderate decrease of 0.41 Å in and $Na_{3-x}AgO_3$. Given that the O−O distance is relatively maintained during sodiation/desodiation process, the formation of π bonding between hole bearing O orbitals remains untrainable.[42, 43] The second factor is that the strong 4d and 2p hybridisation within the entire valence band during the sodiation/desodiation process for all compounds remains mostly unchanged. The formation of σ bonds among the O ions in desodiated compounds necessarily requires a substantial decrease in the 4d-2p hybridisation.[44] By comparing the DOS of the right and left panels of Figure 3, we can see that the 4d-2p hybridisation does not significantly change especially at the bottom of the valence band in all compounds upon desodiation. The strong 4d-2p hybridisation stems from less localised nature of the 4d electrons which facilitates greater hybridisation over large energy bandwidths in the valence band.

It has been established that oxygen redox occurs in materials in which a portion of O 2p states are left unhybridised near the Fermi level.[14] In Li and 3d TM oxides cathode,

electrochemically labile O 2p orbital is usually created by partially substituting the 3d TM ions with either Li or a more electronegative dopant.[14, 45] In These materials that are commonly referred to as cation-disorder and Li excess, O redox acts as a supplementary mechanism that extends the amount of extracted/inserted Li thus increasing their capacity beyond the limits of the TM redox.[16, 44] However, in 4d oxides that we considered here, due to the nature of the 4d-2p hybridisation, electrochemically labile O states are omnipresent during the entire sodiation/desodiation process making the O redox a principal mechanism for charge compensation. For instance, in Na_1NbO_2, under the ideal ionic condition, the top of the valence band should be occupied exclusively by the Nb t_{2g} states while the O states should gravitate towards the bottom of the valence band. The band structure of the more ionic Na_1VO_2, to a great extent, follows this pattern.[40, 46] However, as we saw in Figure 3(c) and (d), O 2p states in Na_1NbO_2 are distributed over the entire valance band and hybridise with Nb t_{2g} states near the Fermi level. As a result, O states donate ~10.71% of the compensated charge during the redox reaction. The same scenario is true for NaP_2O_3 and Na_3AgO_2 which O states are stretched to the top of the valence band and consequently donate electrons during the desodiation. Mixture of TM and O redox has been observed in some 4d TM oxides such as $LiRhO_2$ (Ref. 47), Na_2RuO_3 (Ref. 48) and Li_2RuO_3 (Ref. 49). The participation of O in the redox reaction, in these compounds, is attributed to the great hybridization between the 4d and 2p electrons.[50] This scenario also holds true for the 5d compounds such as Na_2IrO_3.[51] In their 3d iso-structural compounds, however, due to more localised and separated nature of the TM 3d and O 2p states, the TM ion act as the main redox centre.

We identified the ultimate O redox in d^0 compounds $Na_4Zr_5O_{12}$ and Na_2MoO_4 in which the vast majority of redox reaction was carried out on O centres. d^0 compounds such as Li_3NbO_4 been considered electrochemically inactive as the d-shell of their TM ions does not have any available electron for the redox reaction. However, as we demonstrated, $Na_4Zr_5O_{12}$ and

Na_2MoO_4 can undergo reversible Na insertion and extraction solely based on O redox without irreversible O loss. In these compounds, the 4d states, although mostly not available for the redox reaction, provide structural stability through strong hybridisation with O states at the lower energy range in the valence band. This strong hybridisation, in turn, prevents any significant bonding interaction between hole bearing O ions in the compounds and consequently offer structural integrity during the redox reaction.

CONCLUSIONS

We demonstrated that O redox always exists, either mixed with the TM redox or exclusively, in the compounds we studied for Na ion cathode applications. Even in compounds such as $Na_{1-x}Pd_2O_3$ and $Na_{3-x}AgO_2$ where intuitively, TM redox was expected to be dominant, we identified significant participation of the O states in the charge compensation mechanism. The participation of O in these compounds does not stem from Na excess mechanism that has been proposed previously but instead is a by-product of the strong hybridisation between TM 4d and O 2p states. When due to high oxidation state, the 4d TM does not have any electrochemically labile electron, as in $Na_{4-x}Zr_5O_{12}$ and $Na_{2-x}MoO_4$, the O states near the Fermi level bear the burden of the charge compensation while the TM 4d states at the bottom of the valence band stabilise the desodiated compound by preventing irreversible oxygen loss. The concepts developed for d^0 compounds open a new route for designing Na ion cathode materials that do not possess electrochemically labile 4d electrons. The necessary criterion is, however, strong 4d-2p hybridisation at the bottom of the valence band to prevent detrimental O–O bonding.

ACKNOWLEDGEMENTS

This work was supported in part by MEXT as a social and scientific priority issue: Creation of new functional devices and high-performance materials to support next-generation industries to be tackled by using post-K computer. Computational resources were provided

by Kyushu University's high performance computing center and supercomputers at the Institute for Solid State Physics at the University of Tokyo and at the Center for Computational Sciences at University of Tsukuba.

REFERENCES

1. J. B. Goodenough, *Nat. Electron.*, 2018, 1, 204.

2. T. Placke, R. Kloepsch, S. Dühnen and M. Winter, *J. Solid State Electrochem.*, 2017, 21, 1939–1964.

3. M. A. Hannan, M. M. Hoque, A. Mohamed and A. Ayob, *Renew. Sust. Energy Rev.*, 2017, 69, 771–789.

4. Z. P. Cano, D. Banham, S. Ye, A. Hintennach, J. Lu, M. Fowler and Z. Chen, *Nat. Energy*, 2018, 3, 279–289.

5. M. S. Islam and C. A. J. Fisher, *Chem. Soc. Rev.*, 2014, 43, 185–204.

6. P. Canepa, G. Sai Gautam, D. C. Hannah, R. Malik, M. Liu, K. G. Gallagher, K. A. Persson and G. Ceder, *Chem. Rev.*, 2017, 117, 4287–4341.

7. M. D. Slater, D. Kim, E. Lee and C. S. Johnson, *Adv. Funct. Mater.*, 2013, 23, 947–958.

8. A. Pehlken, S. Albach and T. Vogt, *Int. J. Life Cycle Assess.*, 2017, 22, 40−53.

9. R. Schmuch, R. Wagner, G. Hörpel, T. Placke and M. Winter, *Nat. Energy*, 2018, 3, 267–278.

10. N. Tran, L. Croguennec, M. Ménétrier, F. Weill, P. Biensan, C. Jordy and C. Delmas, *Chem. Mater.*, 2008, 20, 4815–4825.

11. D. Liu, J. Han, M. Dontigny, P. Charest, A. Guerfi, K. Zaghib and J. B. Goodenough, *J. Electrochem. Soc.*, 2010, 157, A770–A775.

12. C. Delmas and L. Croguennec, *MRS Bulletin*, 2011, 27, 608–612.

13. K. Nakahara, M. Tabuchi, S. Kuroshima, A. Toda, K. Tanimoto and K. Nakano, *J. Electrochem. Soc.*, 2012, 159, A1398–A1404.

14. A. Grimaud, W. T. Hong, Y. Shao-Horn and J. M. Tarascon, *Nat. Mater.*, 2016, 15, 121–126.

15. M. Saubanere, E. McCalla, J. M. Tarascon and M. L. Doublet, *Energy Environ. Sci.*, 2016, 9, 984–991.

16. B. Qiu, M. Zhang, Y. Xia, Z. Liu and Y. S. Meng, *Chem. Mater.*, 2017, 29, 908–915.

17. Z. Chenglong, W. Qidi, L. Yaxiang, H. Yong-Sheng, L. Baohua and C. Liquan, *J. Phys. D: Appl. Phys.*, 2017, 50, 183001.

18. M. Posternak, R. Resta and A. Baldereschi, *Phys. Rev. B*, 1994, 50, 8911–8914.

19. Y. Moritomo, S. Xu, A. Machida, T. Akimoto, E. Nishibori, M. Takata and M. Sakata, *Phys. Rev. B*, 2000, 61, R7827–R7830.

20. M. S. Whittingham, *Chem. Rev.*, 2004, 104, 4271–4302.

21. N. Ohta, K. Takada, I. Sakaguchi, L. Zhang, R. Ma, K. Fukuda, M. Osada and T. Sasaki, *Electrochem. Commun.*, 2007, 9, 1486–1490.

22. Y. Zhang, E. Zhou, D. Song, X. Shi, X. Wang, J. Guo and L. Zhang, *Phys. Chem. Chem. Phys.*, 2014, 16, 17792–17798.

23. M. T. Naoaki Yabuuchi, Masanobu Nakayama, Hiromasa Shiiba, Masahiro Ogawa, Keisuke Nakayama, Toshiaki Ohta, Daisuke Endo, Tetsuya Ozaki, Tokuo Inamasu, Kei Sato, Shinichi Komaba, *Proc. Natl. Acad. Sci. U.S.A.*, 2015, 112, 7650–7655.

24. M. A. Rzeznik, M. J. Geselbracht, M. S. Thompson and A. M. Stacy, *Angew. Chem. Int. Ed. Engl.*, 1993, 32, 254–255.

25. R. H. Busey and O. L. Keller, *J. Chem. Phys.*, 1964, 41, 215–225.

26. K. H.; and H. R.;, *Z. Anorg. Allg. Chem.*, 1982, 485, 92–100.

27. B. M. Gatehouse and M. C. Nesbit, *J. Solid State Chem.*, 1980, 31, 53–58.

28. Q. Wang, J. H. Sohn, S. Y. Park, J. S. Choi, J. Y. Lee and J. S. Chung, *J. Ind. Eng. Chem.*, 2010, 16, 68–73.

29. R. V. Panin, N. R. Khasanova, C. Bougerol, W. Schnelle, G. Van Tendeloo and E. V. Antipov, *Inorg. Chem.*, 2010, 49, 1295–1297.

30. G. Kresse and J. Furthmüller, *Comput. Mater. Sci.*, 1996, 6, 15–50.

31. G. Kresse and J. Furthmüller, *Phys. Rev. B*, 1996, 54, 11169–11186.

32. S. L. Dudarev, G. A. Botton, S. Y. Savrasov, C. J. Humphreys and A. P. Sutton, *Phys. Rev. B*, 1998, 57, 1505–1509.

33. W. Tang, E. Sanville and G. Henkelman, *J. Phys. Condens. Matter*, 2009, 21, 084204.

34. S. Maintz, V. L. Deringer, A. L. Tchougréeff and R. Dronskowski, *J. Comput. Chem.*, 2016, 37, 1030–1035.

35. M. H. N. Assadi and H. Katayama-Yoshida, *Funct. Mater. Lett.*, 2015, 08, 1540016.

36. C. Sun, J. Liu, Y. Gong, D. P. Wilkinson and J. Zhang, *Nano Energy*, 2017, 33, 363–386.

37. A. Manthiram, X. Yu and S. Wang, *Nat. Rev. Mater.*, 2017, 2, 16103.

38. P. Barpanda, G. Oyama, S.-i. Nishimura, S.-C. Chung and A. Yamada, *Nat. Commun.*, 2014, 5, 4358.

39. Y.-U. Park, D.-H. Seo, H.-S. Kwon, B. Kim, J. Kim, H. Kim, I. Kim, H.-I. Yoo and K. Kang, *J. Am. Chem. Soc.*, 2013, 135, 13870–13878.

40. M. H. N. Assadi and Y. Shigeta, *RSC Adv.*, 2018, 8, 13842–13849.

41. M. H. N. Assadi and Y. Shigeta, *J. Power Sources*, 2018, 388, 1–4.

42. M. Sathiya, G. Rousse, K. Ramesha, C. P. Laisa, H. Vezin, M. T. Sougrati, M. L. Doublet, D. Foix, D. Gonbeau, W. Walker, A. S. Prakash, M. Ben Hassine, L. Dupont and J. M. Tarascon, *Nat. Mater.*, 2013, 12, 827–835.

43. A. M. A. Eric McCalla, Matthieu Saubanère,, E. J. B. Dominique Foix, Gwenaelle Rousse, Marie-Liesse Doublet,, P. N. Danielle Gonbeau, Gustaaf Van Tendeloo, and J.-M. T. Robert Dominko, *Science*, 2015, 350, 1516–1521.

44. D. H. Seo, J. Lee, A. Urban, R. Malik, S. Kang and G. Ceder, *Nat. Chem.*, 2016, 8, 692–697.

45. E. McCalla, M. T. Sougrati, G. Rousse, E. J. Berg, A. Abakumov, N. Recham, K. Ramesha, M. Sathiya, R. Dominko, G. Van Tendeloo, P. Novak and J. M. Tarascon, *J. Am. Chem. Soc.*, 2015, 137, 4804–4814.

46. T. Jia, G. Zhang, Z. Zeng and H. Q. Lin, *Phys. Rev. B*, 2009, 80, 045103.

47. D. Mikhailova, O. M. Karakulina, D. Batuk, J. Hadermann, A. M. Abakumov, M. Herklotz, A. A. Tsirlin, S. Oswald, L. Giebeler, M. Schmidt, J. Eckert, M. Knapp and H. Ehrenberg, *Inorg. Chem.*, 2016, 55, 7079–7089.

48. B. Mortemard de Boisse, G. Liu, J. Ma, S.-i. Nishimura, S.-C. Chung, H. Kiuchi, Y. Harada, J. Kikkawa, Y. Kobayashi, M. Okubo and A. Yamada, *Nat. Commun.*, 2016, 7, 11397.

49. B. Li, H. Yan, Y. Zuo and D. Xia, *Chem. Mater.*, 2017, 29, 2811−2818.

50. M. H. N. Assadi, M. Okubo, A. Yamada and Y. Tateyama, *J. Mater. Chem. A*, 2018, 6, 3747–3753.

51. A. J. Perez, D. Batuk, M. Saubanère, G. Rousse, D. Foix, E. McCalla, E. J. Berg, R. Dugas, K. H. W. van den Bos, M.-L. Doublet, D. Gonbeau, A. M. Abakumov, G. Van Tendeloo and J.-M. Tarascon, *Chem. Mater.*, 2016, 28, 8278–8288.

SUPPLEMENTARY INFORMATION

Tuneable and Reversible O redox in 4d Transition Metal Oxides for high potential Na ion batteries

M. Hussein N. Assadi,[a,b,*] Marco Fronzi,[c,d] Mike Ford[c] and Yasuteru Shigeta[a]

[a]Center for Computational Sciences, University of Tsukuba, Tennodai 1-1-1, Tsukuba, Ibaraki 305-8577, Japan.

[b]Center for Green Research on Energy and Environmental Materials (GREEN), National Institute for Materials Science (NIMS), 1-1 Namiki, Tsukuba, Ibaraki 305-0044, Japan.

[c]International Research Centre for Renewable Energy, State Key Laboratory of Multi- phase Flow in Power Engineering, Xi'an Jiaotong University, Xi'an 710049, Shaanxi, China.

[d]School of Mathematical and Physical Science, University of Technology Sydney, Ultimo 2007, New South Wales 2007, Australia.

[*]Email: h.assadi.2008@ieee.org

1. Additional Computational Settings

The pseudopotentials used in calculations contained the following electrons: $2s^2 2p^4$ for O; $2p^6 3s^1$ for Na, $4p^6 4d^4 5s^1$ for Nb, $4p^6 4d^5 5s^1$ for Mo; $4p^6 4d^{10}$ for Pd; and $4d^{10} 5s^1$ for Ag. The special capacity ($Q_{Theoretical}$) in mAh/g was calculated according to following formula:

$$Q_{Theoretical} = \frac{n\mathcal{F}}{3600 M_{Molecular}} \qquad \text{Equation 1.}$$

Here, n is the extracted charge, $\mathcal{F}$ is the Faraday constant (96485.3329 sA/mol), and $M_{Molecular}$ is the molecular weight in g/mole. The capacity was calculated by multiplying the special capacity in the cell voltage.

2. Structural Details

The Na_1NbO_2 and Na_3AgO_2 compounds have been previously synthesised and characterised [1,2]. Tables S1 and S2 present the calculated and experimental lattice parameters for these two compounds. The calculated and measured lattice parameters differ only by ~1% indicating excellent convergence of the DFT calculation within the GGA+U framework.

Table S1. The calculated and experimental lattice parameters of Na_1NbO_2.

Na_1NbO_2	Calculated	Experimental
Lattice Group	194 ($P6_3/mmc$)	194 ($P6_3/mmc$)
a (Å)	3.013	2.955
b (Å)	3.013	2.955
c (Å)	11.708	11.647
α (°)	90.000	90
β (°)	90.000	90
γ (°)	120.000	120

Table S2. The calculated and experimental lattice parameters of Na_3AgO_2.

Na_3AgO_2	Calculated	Experimental
Lattice Group	72 ($Ibam$)	72 ($Ibam$)
a (Å)	5.525	5.463
b (Å)	11.031	10.926
c (Å)	6.002	5.926
α (°)	90.000	90
β (°)	90.000	90
γ (°)	90.000	90

Monoclinic Na_2MoO_4 has been synthesised [3]. Its structure, however, has not been fully characterised yet. We, nonetheless, present a comparison between the calculated Na_2MoO_4 lattice parameters and the lattice parameter of the isostructural monoclinic K_2MoO_4 [4] in Table S3. The lattice constants of Na_2MoO_4 are ~5% smaller than those of K_2MoO_4. This shrinkage can be attributed to the smaller ionic radius of Na^+ compared to that of K^+.

Table S3. Comparison between the calculated lattice parameters of Na_2MoO_4 with the experimental lattice parameters of K_2MoO_4.

Na_2MoO_4	Calculated Na_2MoO_4	Experimental K_2MoO_4
Lattice Group	12 ($C2/m$)	12 ($C2/m$)
a (Å)	11.692	12.348
b (Å)	5.945	6.081
c (Å)	6.942	7.538
α (°)	90.000	90
β (°)	117.647	115.74
γ (°)	90.000	90

$Na_4Zr_5O_{12}$ and $Na_1Pd_2O_3$ have not yet been synthesis. We modelled these compounds after the synthesised and well-characterised $K_4Zr_5O_{12}$ and KPd_2O_3 [5-7]. Tables S4 and S5 present a comparison between the Na based and K based compounds. The c value is 2.01% shorter in $Na_4Zr_5O_{12}$ than in $K_4Zr_5O_{12}$. The difference is more profound in the palladate compounds as the c is 11.12% smaller in sodium palladate than in potassium palladate.

Table S4. Comparison between the calculated lattice parameters of $Na_4Zr_5O_{12}$ with the experimental lattice parameters of $K_4Zr_5O_{12}$.

	$Na_4Zr_5O_{12}$ (Calculated)	$K_4Zr_5O_{12}$ Experimental
Lattice Group	164 ($P\bar{3}m1$)	164 ($P\bar{3}m1$)
a (Å)	5.855	5.821
b (Å)	5.855	5.821
c (Å)	10.652	10.437
α (°)	90.000	90
β (°)	90.000	90
γ (°)	120.000	120

Table S5. Comparison between the calculated lattice parameters of $Na_1Pd_2O_3$ with the experimental lattice parameters of $K_1Pd_2O_3$.

	$Na_1Pd_2O_3$ (Calculated)	$K_1Pd_2O_3$ (Experimental)
Lattice Group	160 ($R3m$R3m)	160 ($R3m$)
a (Å)	6.130	6.073
b (Å)	6.130	6.073
c (Å)	16.897	18.777
α (°)	90.000	90
β (°)	90.000	90
γ (°)	120.000	120

Since $Na_4Zr_5O_{12}$ and $Na_1Pd_2O_3$ have not been synthesised yet, we examined their stability against the binary oxides they may decompose to. The results are presented in Table S6. Negative formation enthalpy (ΔH)

indicates the stability of the ternary compounds. According to Table S6 both $Na_4Zr_5O_{12}$ and $Na_1Pd_2O_3$ were found energetically stable against decomposing into the competing binary oxides.

Table S6. The formation enthalpy (ΔH) of the ternary oxides with respect to the binary oxides.

compound	ΔH(eV/u.f.)	Competing oxide phases
$Na_4Zr_5O_{12}$	−8.241	$5ZrO_2+2Na_2O$
$Na_1Pd_2O_3$	−4.177	$2PdO+½Na_2O+¼O_2$

3. Choice of Functional

The conventional and popular general gradient approximation (GGA) is known to overly delocalise the *d* states and underestimate bang gaps of the transition metal (TM) oxides [8]. Since the localisation effects are stronger for 3*d* electrons, these problem manifest most adversely in 3d TM oxides. However, in the 4d TM oxides we studied here, localisation effects are rather smaller and the shortcoming of the GGA method can be mitigated by introducing a modest Hubbard term on the 4*d* electrons. In our work, we choose a U_{eff} value of 2 eV for all TM ions. The choice of a single value U_{eff} allowed us a straightforward comparison of the materials properties. In Figure S1, present the DOS of the sodiated and desodiated compounds calculated under the GGA functional. For most of the compounds the GGA DOS is approximately similar to the one calculated with GGA+U functional (Figure 3). Noticeable differences however occur in $Na_{0.5}Pd_2O_3$ for which the position of the Fermi level is wrongly placed in the middle of valence band in GGA calculations. Table S7, presents the half-cell voltages calculated with GGA functional and the GGA+U (U_{eff} = 2 eV). Evidently, GGA+U methods introduces a moderate correction with respect to the mere GGA method.

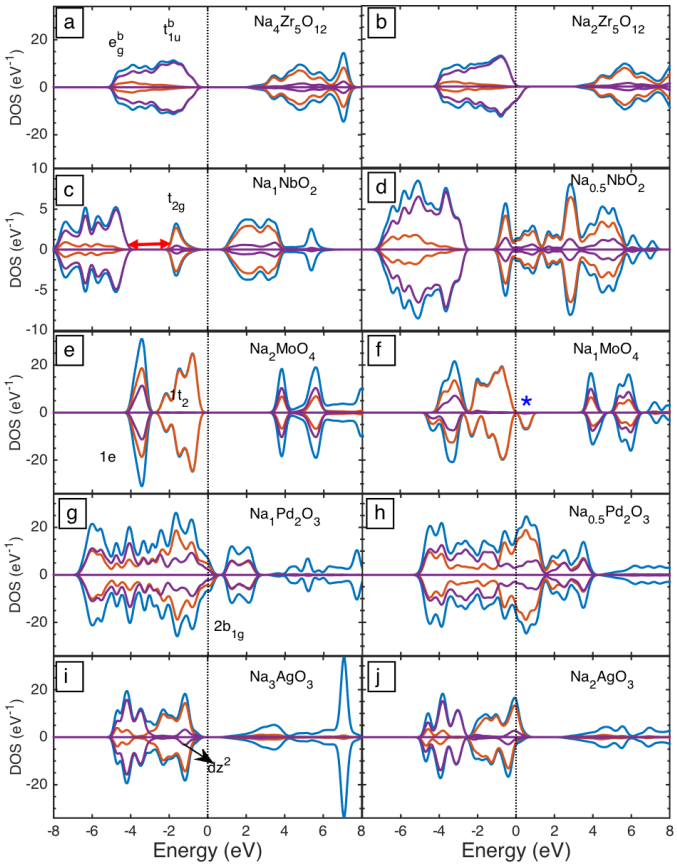

Figure S1. The total and partial density of states of the sodiated (left column) and desodiated compounds (right column) calculated with GGA method. Blue, purple and orange lines represent total, O 2p and TM 4d partial states respectively.

Table S7. Voltages calculated with GGA+U and GGA functionals.

	$Na_{4-x}Zr_5O_{12}$	$Na_{1-x}NbO_2$	$Na_{2-x}MoO_4$	$Na_{1-x}Pd_2O_3$	$Na_{3-x}AgO_2$.
Potential (V) GGA+U	3.583	2.476	4.743	2.630	2.398
Potential (V) GGA	3.790	2.247	4.369	2.666	2.314

To examine the how the DOS is influenced if we chose a higher U_{eff} value or higher level functional, we calculated the DOS of the Na_2MoO_4 compound with U_{eff} = 3.7 eV and the hybrid HSE06 functional [9,10] with a mixing parameter α = 0.2, presented in Figure S1(b) and (c) respectively. U_{eff} value of 3.7 eV was used for Na_2MoO_4 in Materials Project. As we can see in Figure 2S, the dominance of O 2p states near the valence band maximum is a preserved feature for all functional used. Furthermore, the calculated bandgap (E_g) does not strongly depend on the functional chosen indicating that U_{eff} value we used in the calculation was adequate for these 4d TM oxides.

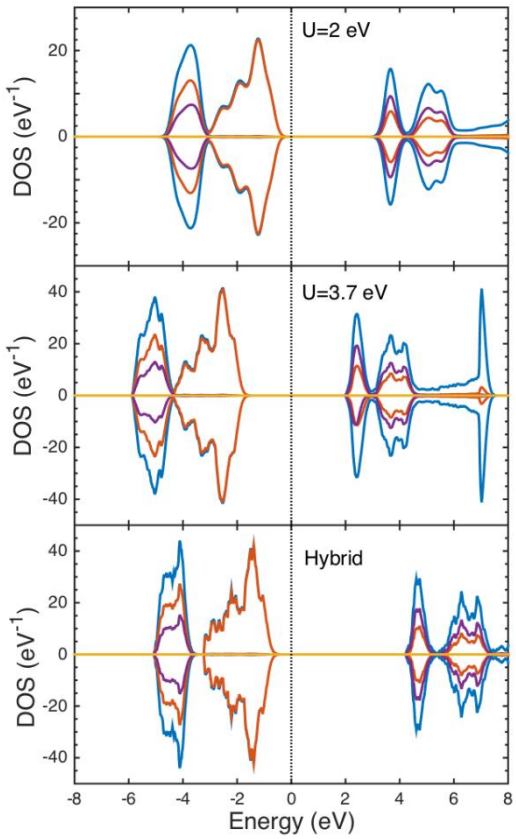

Figure S2. The total and partial density of states of the Na_2MoO_4 compound calculated with various functionals. Blue, purple and orange lines represent total, O 2p and TM 4d partial states respectively.

References

1 Hans-Friedrich, R., Gerd, M., Zhiwei, H. & Günter, K. Synthesis, structure, and X-ray absorption spectra of Li_xNbO_2 and Na_xNbO_2 (x≤1). *Z. Anorg. Allg. Chem.* **619**, 1369–1373, doi:doi:10.1002/zaac.19936190808 (1993).

2 Klassen, H. & Hoppe, R. Alkalioxoargentate(I). Über Na_3AgO_2. *Z. Anorg. Allg. Chem.* **485**, 92–100, doi:doi:10.1002/zaac.19824850109 (1982).

3 Busey, R. H. & Keller, O. L. Structure of the Aqueous Pertechnetate Ion by Raman and Infrared Spectroscopy. Raman and Infrared Spectra of Crystalline $KTcO_4$, $KReO_4$, Na_2MoO_4, Na_2WO_4, $Na_2MoO_4{\cdot}2H_2O$, and $Na_2WO_4{\cdot}2H_2O$. *J. Chem. Phys.* **41**, 215–225, doi:10.1063/1.1725625 (1964).

4 Gatehouse, B. M. & Leverett, P. Crystal structure of potassium molybdate, K_2MoO_4. *J. Chem. Soc. A*, 849–854, doi:10.1039/J19690000849 (1969).

5 Gatehouse, B. M. & Nesbit, M. C. The crystal structure of the 2:5 phase in the K_2O-ZrO_2 system: $K_4Zr_5O_{12}$, a compound with octahedral and trigonal prismatic zirconium(IV) coordination. *J. Solid State Chem.* **31**, 53–58, doi:10.1016/0022-4596(80)90007-9 (1980).

6 Wang, Q. *et al.* Preparation and catalytic activity of $K_4Zr_5O_{12}$ for the oxidation of soot from vehicle engine emissions. *J. Ind. Eng. Chem.* **16**, 68–73, doi:10.1016/j.jiec.2010.01.019 (2010).

7 Panin, R. V. *et al.* Ordering of Pd^{2+} and Pd^{4+} in the mixed-valent palladate KPd_2O_3. *Inorg. Chem.* **49**, 1295–1297, doi:10.1021/ic902187a (2010).

8 Pribram-Jones, A., Gross, D. A. & Burke, K. DFT: A Theory Full of Holes? *Annu. Rev. Phys. Chem.* **66**, 283–304, doi:10.1146/annurev-physchem-040214-121420 (2015).

9 Heyd, J., Scuseria, G. E. & Ernzerhof, M. Hybrid functionals based on a screened Coulomb potential. *J. Chem. Phys.* **118**, 8207–8215, doi:10.1063/1.1564060 (2003).

10 Heyd, J., Scuseria, G. E. & Ernzerhof, M. Erratum: “Hybrid functionals based on a screened Coulomb potential” [J. Chem. Phys. 118, 8207 (2003)]. *J. Chem. Phys.* **124**, 219906, doi:10.1063/1.2204597 (2006).